

Quasiparticle Dynamics in the 4d–4f Ising-like Double Perovskite Ba₂DyRuO₆ Probed by Neutron Scattering and Machine-Learning Framework

G. Roy,^{1,*} E. Kushwaha,¹ M. Kumar,¹ S. Ghosh,¹ F. Orlandi,² M. D. Le,² M. B. Stone,³ J. Sannigrahi,⁴ D. T. Adroja,^{2,5} and T. Basu^{1,†}

¹*Rajiv Gandhi Institute of Petroleum Technology, Jais, Amethi, 229304, India*

²*ISIS Neutron and Muon Source, STFC, Rutherford Appleton Laboratory, Harwell campus, Didcot, Oxfordshire OX11-0QX, United Kingdom*

³*Neutron Scattering Division, Oak Ridge National Laboratory, Oak Ridge, Tennessee 37831, USA*

⁴*School of Physical Sciences, Indian Institute of Technology Goa, Farmagudi, Goa 403401, India*

⁵*Highly Correlated Matter Research Group, Physics Department, University of Johannesburg, Auckland Park 2006, South Africa*

Double perovskites containing 4d–4f interactions provide a platform to study complex magnetic phenomena in correlated systems. Here, we investigate the magnetic ground state and quasiparticle excitations of the fascinating double perovskite system, Ba₂DyRuO₆, through Time of flight (TOF) neutron diffraction (TOF), inelastic neutron scattering (INS), and theoretical modelling. The compound Ba₂DyRuO₆ is reported to exhibit a single magnetic transition, in sharp contrast to most of the other rare-earth (R) members in this family, A₂RRuO₆ (A = Ca/Sr/Ba), which typically show magnetic ordering of the Ru ions, followed by R-ion ordering. Our neutron diffraction results confirm that long-range antiferromagnetic order emerges at $T_N \approx 47$ K, primarily driven by 4d–4f Ru⁵⁺–Dy³⁺ exchange interactions, where both Dy and Ru moments start to order simultaneously. The ordered ground state is a collinear antiferromagnet with Ising character, carrying ordered moments of $\mu_{Ru} = 1.6(1) \mu_B$ and $\mu_{Dy} = 5.1(1) \mu_B$ at 1.5 K. Low-temperature INS reveals well-defined magnon excitations below 10 meV. SpinW modelling of the INS spectra evidences complex exchange interactions and the presence of magnetic anisotropy, which governs the Ising ground state and accounts for the observed magnon spectrum. Combined INS and Raman spectroscopy reveal crystal-electric-field (CEF) excitations of Dy³⁺ at 46.5 and 71.8 meV in the paramagnetic region. The observed CEF levels are modelled through point-charge CEF calculations, consistent with the O_h site symmetry of Dy³⁺. A complementary machine-learning approach is used to calculate and analyse the phonon spectrum, enabling a direct comparison with the INS data. These combined experimental and theoretical results provide a comprehensive understanding of the origin of phonon and magnon quasiparticle excitations and their influence on the crystal structure and ground-state magnetism of Ba₂DyRuO₆.

I. INTRODUCTION

The strong d – f interactions in rare-earth (R) transition-metal (M) oxides provide valuable insights into exotic magnetic and electronic properties[1–9]. While 3d–4f systems have been extensively studied [1, 5–8, 10], materials incorporating both rare-earth (R) and 4d/5d transition metal (TM) ions have received comparatively less attention. In particular, the 4d–4f coupling benefits from enhanced hybridization, strong spin-orbit coupling (SOC), and crystal electric field (CEF) effects of the 4d orbitals combined with rare-earth anisotropy of f -orbitals, leading to unconventional magnetic ground states[2, 11, 12]. The interplay between all these key factors enables the design of tunable magnetic materials, advancing research in quantum magnetism. For example, the 4d–4f pyrochlore systems, R₂Ru₂O₇ (R = Y, Pr, Nd, Gd, Dy, Ho, etc.), exhibit fascinating magnetic ground states at different temperatures, such as spin-frustrated states and spin-ice behavior, with differ-

ent magnetic ground states for different R-ions [7, 15–17]. Recent studies on the 6H-perovskite Ba₃RRu₂O₉ document versatile physical properties and intriguing magnetic ground states for different rare-earth members, such as cooperative magnetic ordering of R and Ru moments [2, 11–13], spin-driven ferroelectricity for the Ho member [11, 18, 19], an unusual +4 valence state for Tb [12], and most surprisingly, ferromagnetic ordering of Nd in the Ba₃NdRu₂O₉ compound [20]. The versatile behavior could result from differing degrees of 4d–4f hybridization and lattice distortion, both of which play decisive roles in determining the exchange interactions.

Double perovskites with larger d orbitals (4d/5d) have gained additional attention, as they exhibit a variety of rich phenomena such as spin frustration, high-temperature ordering via double exchange interactions, field-induced magnetism, and magnetoresistance [14, 21–27]. In particular, the A₂LnRuO₆ series (A = alkali metal; Ln= Y, La, Lu (nonmagnetic) or rare-earth ions Ce–Yb (magnetic)) shows exotic ground states arising from spin frustration and complex magnetic exchange interactions driven by A-site and Ln-site cation variations [14, 28–37]. For instance, Sr₂LnRuO₆ (Ln = Dy, Ho, Er) crystallizes in the monoclinic space group $P2_1/n$ with two phase transitions, exhibiting exchange-

* gourabr22bs@rgipt.ac.in

† tathamay.basu@rgipt.ac.in

bias properties that may arise due to the Dzyaloshinskii–Moriya (DM) interaction in such low-symmetry crystal structures [32]. In contrast, substituting nonmagnetic Y^{3+} for Ln, while retaining the same space group, reveals planar AFM correlations above 24 K and a partially ordered state between 24–32 K, attributed to geometrical frustration inherent to the lattice [14]. Moreover, in such double perovskites, the nonmagnetic alkaline-earth metal ($A = \text{Ba}, \text{Sr}, \text{Ca}$) plays a pivotal role in the structural stability and electronic environment, which in turn vastly modifies the magnetic exchange interactions, yielding a completely different magnetic ground state for different A-ion. For example, most Sr-based double perovskites discussed above, such as Sr_2RRuO_6 ($R = \text{Y}, \text{Dy}, \text{Ho}, \text{Er}, \text{Tb}$), crystallize in the monoclinic space group $P2_1/n$ [14, 32–35]. When Sr is replaced by the larger Ba atom, such as, $\text{Ba}_2\text{DyRuO}_6$ [29], $\text{Ba}_2\text{HoRuO}_6$ [30], Ba_2YRuO_6 [36], the system crystallises in a highly symmetric Fm-3m cubic structure, with the only exception of $\text{Ba}_2\text{PrRuO}_6$ [31], which crystalline in a monoclinic space group $P2_1/n$. However, in all these cubic systems the magnetic ground-state remains poorly understood. Given their wide range of technological applications, it is important to explore how changing each element—either A (nonmagnetic) or B (magnetic)—can significantly alter the crystal structure, and how the associated symmetries strongly influence the ground-state magnetic properties in this diverse group of materials.

$\text{Ba}_2\text{DyRuO}_6$ crystallizes in a cubic structure with space group Fm-3m [29]. It exhibits a single magnetic ordering transition at 47 K, in sharp contrast to the previously discussed R ions in the same family, where two distinct ordering temperatures were observed [29]. The ground states of Ru and Dy in this compound remain unexplored. Here, we investigate this system using time-of-flight neutron powder diffraction (NPD), inelastic neutron scattering (INS), and modelling the magnetic (or spin wave) excitations using SPINW simulations [38]. Additionally, theoretical simulations and machine-learning methods were employed to understand the crystal electric field (CEF) and Phonon excitations in this system. By examining these results collectively, we have estimated the nearest- and next-nearest-neighbour exchange interactions and magnetic anisotropy, modelling the INS spectra with SPINW simulations. Such a comprehensive investigation is scarce in the literature for this entire series.

II. EXPERIMENTAL DETAILS

The polycrystalline sample $\text{Ba}_2\text{DyRuO}_6$ is prepared by solid-state reaction by mixing and grinding BaCO_3 , Dy_2O_3 , and RuO_2 in a mortar and pestle in the proper ratio [29]. The sample is initially heated at 960°C for 24 hours in the first step. The final sintering is performed on the pelletized sample at 1140°C for 24 hours with several intermediate mixing and grinding of the sample

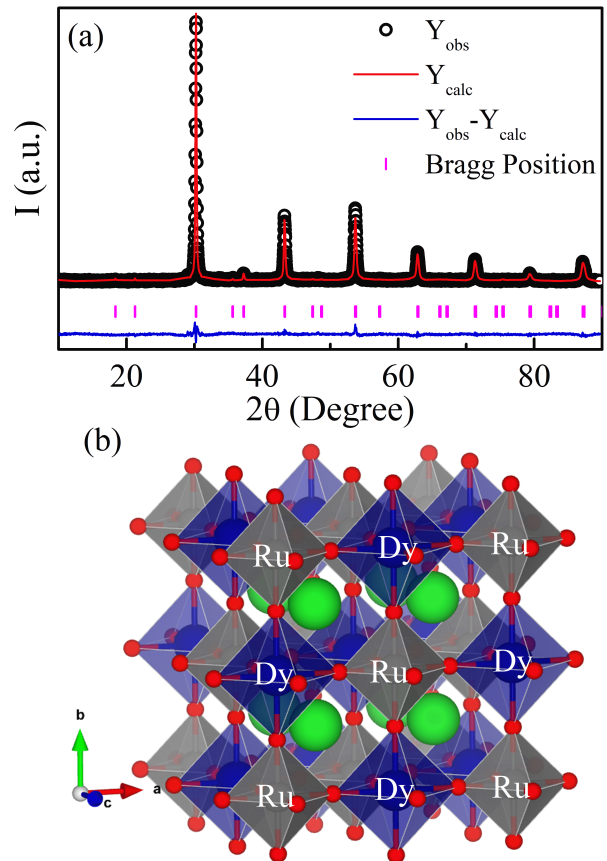


FIG. 1. (a) Rietveld refinement of the X-ray diffraction (XRD) pattern of $\text{Ba}_2\text{DyRuO}_6$ measured at room temperature, with intensity (I) plotted as a function of 2θ ($^\circ$). Open black circles represent the observed data, the solid red line corresponds to the calculated pattern, vertical pink ticks indicate Bragg reflection positions, and the blue line at the bottom shows the difference between observed and calculated intensities. (b) Crystal structure of $\text{Ba}_2\text{DyRuO}_6$ crystallizing in the cubic Fm-3m space group. Red spheres represent oxygen sites and green spheres represent barium sites.

to obtain a uniform homogenised sample. Then, powder X-ray diffraction (XRD) patterns were recorded at room temperature using Cu $K\alpha$ radiation ($\lambda = 1.5406 \text{ \AA}$) on a PANalytical Empyrean diffractometer at RGIPT, India. The room-temperature Rietveld refinement (FIG. 1(a)), performed using the FullProf Suite [39], confirms that the sample forms in the desired phase, crystallizing in the cubic Fm-3m space group (FIG. 1(b)), consistent with earlier reports [29]. The Dy^{3+} and Ru^{5+} ions occupy the Wyckoff positions $4b$ and $4a$, respectively, in a 1:1 ratio. The lattice parameters obtained from the refinement are $a = b = c = 8.345(2) \text{ \AA}$ and $\alpha = \beta = \gamma = 90^\circ$, consistent with the earlier report [29]. Neutron Powder Diffraction (NPD) is performed using the high-flux and high-resolution Time-of-Flight WISH Diffractometer at ISIS, UK [40]. The 4.5 g sample was packed in a sealed vanadium annular can for the NPD measure-

ments. Initially, room-temperature data were taken, and then the sample was cooled using a liquid He cryostat. The low-temperature NPD data were collected during heating from 1.5 K to 250 K. The refinement and analysis of NPD data were carried out using the FullProf [39], BASIREPS [41], VESTA [42] software packages and Bilbao crystallographic server for magnetic space group [43]. Inelastic neutron scattering study was conducted on the MARI spectrometer at ISIS, UK, using a 3 g sample in an aluminium canister [44]. The incident neutron energy was set at $E_i = 180$ meV (with additional measurements at 100, 29.7, 22.9, and 11.7 meV) in Repetition Rate Multiplication (RRM) mode, with a Gd-Fermi chopper operating at 400 Hz. Data were collected at temperatures of 5 K, 30 K, and 100 K. The analysis of INS data was performed using the Mantid and Dave software packages [45, 46]. Further theoretical modelling was carried out using SpinW, a MATLAB-based library [38]. SpinW numerically computes and visualises the spin-wave dispersion by employing linear spin wave theory, incorporating the spin Hamiltonian, magnetic structure, and structural and magnetic twinning effects. The Raman spectrum was recorded at room temperature using a 532 nm excitation laser, a 1200 grooves/mm grating, 100 accumulations, and a spectral range of 200–2000 cm^{-1} at 1 cm^{-1} resolution, employing the Central Instrumentation Facility (CIF) at Rajiv Gandhi Institute of Petroleum Technology (RGIPT). Phonon calculations were carried out using the INSPIRED software [47], which employs pre-trained machine learning force fields (MLFFs) derived from the MatterSim modeling package. The optimized structure and momentum-dependent phonon modes were subsequently obtained [48].

III. RESULTS AND DISCUSSIONS

A. Neutron Powder Diffraction

Neutron powder diffraction (NPD) measurements were performed on $\text{Ba}_2\text{DyRuO}_6$ at several temperatures down to 1.5 K to determine the ground state magnetic structure. The Rietveld refinements at 300 K in the low- Q range ($0.65 \leq Q \leq 2 \text{ \AA}^{-1}$) and the high- Q range ($2 \leq Q \leq 12 \text{ \AA}^{-1}$) are shown in FIGs. 3(b) and 3(d), while the corresponding refinements at 1.5 K are shown in FIGs. 3(a) and 3(c). Initially, the 300 K data were refined to determine the crystal structure, followed by the 1.5 K data to explore the magnetic structure. The cell parameters, atomic positions, thermal parameters, and occupancies of the nuclear structure obtained from the Rietveld refinement are listed in Table I for 1.5 K and 300 K. The neutron absorption of Dy was properly accounted for during the refinement by using an empirical exponential correction, ensuring accurate estimation of both the crystal and magnetic structures. Examination of diffraction patterns between 1.5 K, 15 K, 30 K, 45 K, and above the ordering temperature (55 K) reveals the

presence of pure magnetic reflections at $Q = 0.75, 1.06, 1.68, 1.84, 2.24, 2.38, 2.72, 2.81, 3.09, 3.19, 3.44, 3.53, 3.76, 3.82, 4.04, 4.12$ and 4.62 \AA^{-1} , as shown in FIG. 2. These additional reflections violate the F -centring extinction conditions and can be consistently indexed using the magnetic propagation vector $\mathbf{k} = (0, 1, 0)$ [49].

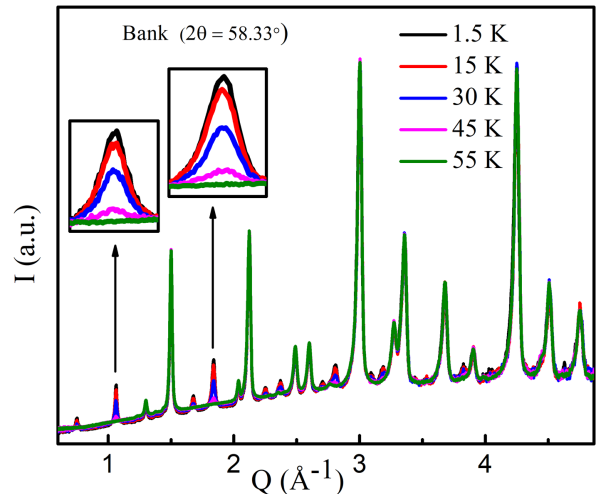


FIG. 2. Comparison of neutron powder diffraction (NPD) patterns collected at 1.5 K, 15 K, 30 K, 45 K, and 55 K, with intensity I plotted as a function of momentum transfer Q (\AA^{-1}), highlighting the magnetic reflections from the WISH bank with average $2\theta = 58.33^\circ$. The inset shows an enlarged view of the two prominent magnetic peaks at $Q = 1.06$ and 1.84 \AA^{-1} .

TABLE I. Atomic coordinates of $\text{Ba}_2\text{DyRuO}_6$ (space group $Fm\text{-}3m$) at 1.5 K and 300 K.

1.5 K						
(Cell parameters: $a = b = c = 8.3434(3) \text{ \AA}$, $\alpha = \beta = \gamma = 90^\circ$)						
Atom (Site)	x	y	z	B_{iso}	Occupancy	
O (24e)	0.2349(3)	0.0000	0.0000	0.7066(4)	0.1250(2)	
Ru(4a)	0.0000	0.0000	0.0000	0.2241(4)	0.0208(1)	
Ba (8c)	0.2500	0.2500	0.2500	0.3764(1)	0.0416(3)	
Dy (4b)	0.5000	0.5000	0.5000	0.2241(2)	0.0208(2)	
300 K						
(Cell parameters: $a = b = c = 8.3562(4) \text{ \AA}$, $\alpha = \beta = \gamma = 90^\circ$)						
Atom (Site)	x	y	z	B_{iso}	Occupancy	
O (24e)	0.2351(3)	0.0000	0.0000	1.1888(5)	0.1250(2)	
Ru(4a)	0.0000	0.0000	0.0000	0.3275(3)	0.0208(1)	
Ba (8c)	0.2500	0.2500	0.2500	0.9252(2)	0.0416(2)	
Dy (4b)	0.5000	0.5000	0.5000	0.3275(3)	0.0208(1)	

The cubic metric of the unit cell does not allow a unique determination of the moment direction with respect to the nuclear structure from powder data. The only reliable information that can be extracted is whether

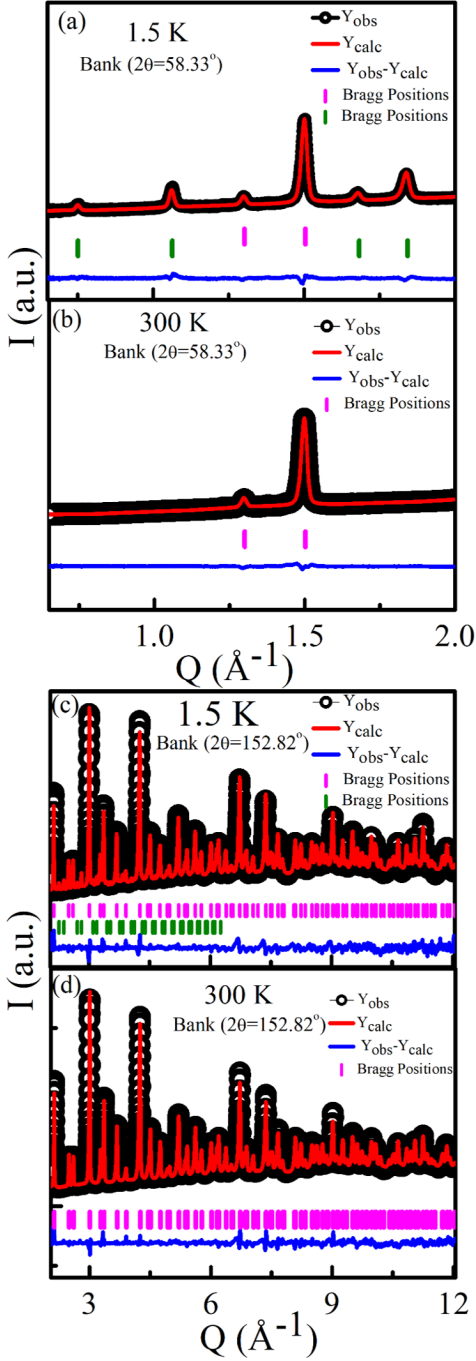


FIG. 3. (a) Rietveld refinement of neutron diffraction data from the WISH Bank with average $2\theta = 58.33^\circ$ collected at 1.5 K, and (b) at 300 K in the range $0.65 \leq Q \leq 2 \text{ \AA}^{-1}$. Open black circles show the observed pattern, and the solid red line is the calculated profile. Vertical purple and green ticks indicate the nuclear (top) and magnetic (bottom) Bragg positions, respectively, while the blue curve represents the difference between the observed and calculated intensities. (c) Rietveld refinement of neutron diffraction data from the WISH Bank with average $2\theta = 152.82^\circ$ collected at 1.5 K, and (d) at 300 K in $2 \leq Q \leq 12 \text{ \AA}^{-1}$.

the magnetic moments lie parallel or perpendicular to the propagation vector. Preliminary refinements indicate that the moments lie in the plane perpendicular to the propagation vector \mathbf{k} . To further investigate the moment orientation, we examined the magnetic space groups derived from the parent space group Fm-3m (No. 225) [50]. Among the magnetic space groups obtained from a single irreducible representation and a single arm of the star of \mathbf{k} , only four groups— $P14/mnc$, C_{Amca} , $P1n1m$ and $Pa2_1/c$ —permit nonzero magnetic moments on both Ru^{5+} and Dy^{3+} sites. The $P14/mnc$ subgroup corresponding to the $mX3^+$ irreducible representation allows a moment parallel to the propagation vector (in our case along the b direction of the parent cubic structure), C_{Amca} allows a moment along the a axis, and $P1n1m$ allows a moment along the $[110]$ direction within the ac plane of the parent structure, whereas the $Pa2_1/c$ magnetic space group allows the moment to lie in a general direction within the ac plane of the cubic structure. The latter three space groups correspond to the $mX5^+$ irreducible representation with different order-parameter directions. The magnetic refinement shows that the moments cannot be fitted exclusively along the b axis, thus ruling out the $P14/mnc$ subgroup. Regarding the remaining three magnetic space groups, these cannot be distinguished from the powder data due to the cubic metric of the unit cell. For this reason, we have arbitrarily chosen to place the moment along the $[110]$ direction of the parent cubic unit cell, corresponding to the $P1n1m$ magnetic space group. The latter is defined in a unit cell related to the cubic parent structure by the transformation

$$\left\{ (0, 1, 0), \left(-\frac{1}{2}, 0, \frac{1}{2}\right), \left(\frac{1}{2}, 0, \frac{1}{2}\right) \right\}$$

with the same origin choice. If the equivalent propagation vectors $\mathbf{k} = (1, 0, 0)$ or $\mathbf{k} = (0, 0, 1)$ are considered, equally good fits are obtained for moment orientations within the bc and ab planes, respectively, corresponding to the different domains of same magnetic space group $P1n1m$. The magnetic structure is shown in FIG. 4 using the parent structure unit cell for clarity. The magnetic moments at 1.5 K are found to be $\mu_{\text{Ru}^{5+}} = 1.6(1) \mu_B$ and $\mu_{\text{Dy}^{3+}} = 5.1(1) \mu_B$, obtained from the Rietveld refinement as shown in FIG. 3(a) and (c).

For the monoclinic ($P2_1/n$) compound $\text{Ba}_2\text{PrRuO}_6$, the Ru and Pr moments lie in the ac plane, but the moments are non-collinear [31]. In $\text{Ba}_2\text{PrRu}_{0.9}\text{Ir}_{0.1}\text{O}_6$, the Pr moments align along the c axis, whereas the Ru moments lie within the ac plane [31]. In $\text{Ba}_2\text{HoRuO}_6$ [30], the magnetic moments are oriented along the c direction. Even when only the A site of the double perovskite $A_2BB'O_6$ is substituted, substantial changes are observed in both the crystal and magnetic structures. For example, in $\text{Sr}_2\text{DyRuO}_6$ (monoclinic space group $P2_1/n$) [34], the moments align along the b direction. In $\text{Sr}_2\text{HoRuO}_6$ (also $P2_1/n$) [33], both Ru and Ho moments align along the c direction. In $\text{Sr}_2\text{ErRuO}_6$, the magnetic

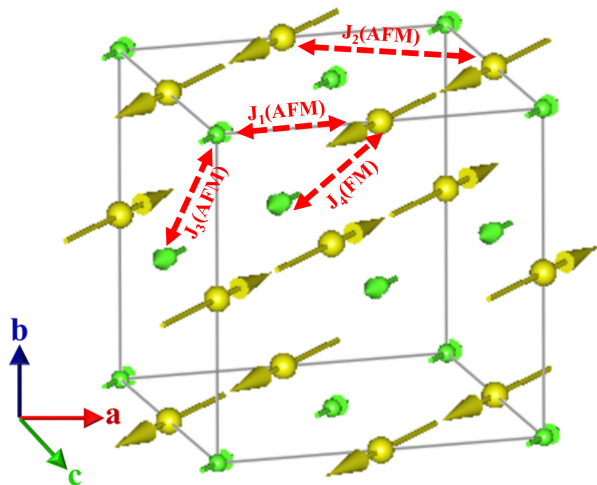


FIG. 4. Magnetic ground state of $\text{Ba}_2\text{DyRuO}_6$ at 1.5 K, drawn in the cubic unit cell of the parent structure showing a collinear magnetic structure within the ac plane with propagation vector $\mathbf{k} = (0, 1, 0)$. Yellow spheres represent Dy atoms, and green spheres represent Ru atoms. The dominant exchange path is indicated by red dotted lines.

structure features Er^{3+} and Ru^{5+} moments that remain predominantly aligned along the c axis while exhibiting a slight tilt away from perfect collinearity [35]. Interestingly, in $\text{Sr}_2\text{YbRuO}_6$ [37], the moments of both Yb and Ru are arranged in a coplanar configuration within the ab plane. These findings suggest that substituting either the A -site alkaline-earth ions or different rare-earth elements exerts a profound influence on the orientation and interaction of the Ru and rare-earth magnetic moments.

The temperature dependence of the magnetic moment variation of Ru^{5+} and Dy^{3+} , obtained from Rietveld refinement of time-of-flight neutron diffraction data, is shown in FIG. 5(a), with the normalised moment in FIG. 5(b). These results confirm the magnetic ordering $T_N = 47(1)$ K, consistent with the value reported for bulk [29]. In $\text{Ba}_2\text{DyRuO}_6$, the Ru^{5+} moments saturate earlier than the Dy^{3+} moments. (see FIG. 5(b)). This result is consistent with other similar Ru-based double perovskite systems [34]. FIG. 5(c) shows the plot of the integrated intensity (I) of the strongest magnetic peak (peak located at $Q = 1.84 \text{ \AA}^{-1}$ from FIG. 2) at various temperatures below the ordering temperature. The estimated critical exponent $\beta = 0.325(2)$ is consistent with a 3D Ising-nature of moments [51].

B. Inelastic Neutron Scattering

To understand phonon and magnon excitations, the crystal electric field (CEF), and to interpret the magnetic ground state, we performed inelastic neutron scattering (INS) experiments at various incident energies. FIG.6(a)–(c) color contour plots describing low-energy

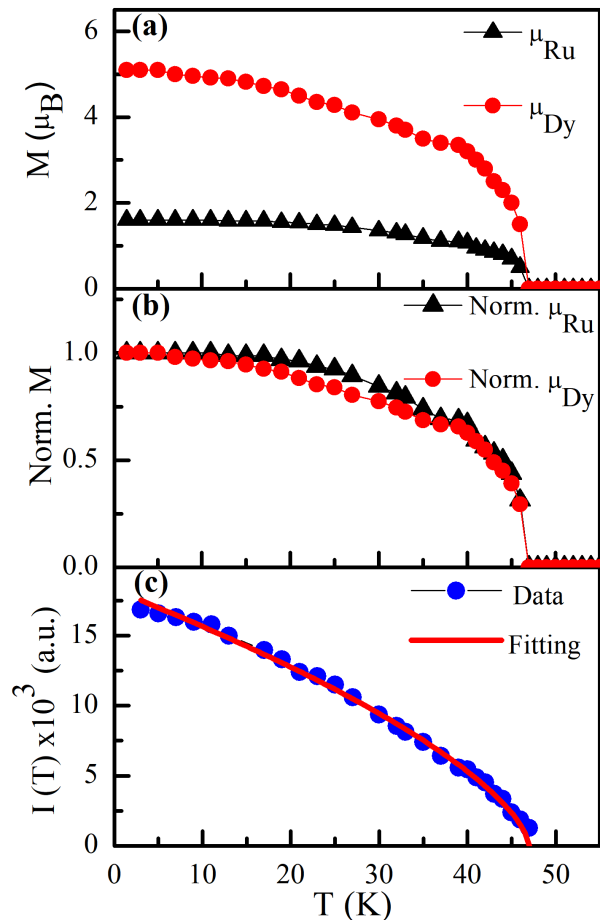


FIG. 5. Thermal variation of (a) Dy^{3+} and Ru^{5+} moments based on refinement, (b) normalised moments of Dy^{3+} and Ru^{5+} , and (c) temperature dependence of the integrated intensity $I(T)$ below the ordering temperature. A uniform uncertainty of $\pm 0.1 \mu_B$ is considered for the refined magnetic moments. The data are fitted with $I(T) = I_0(1 - T/T_N)^{2\beta}$ using $\beta = 0.325(2)$ (Ising model).

excitations in the Q region 0.5 to 4.0 \AA^{-1} , recorded at temperatures of 5 K, 30 K, and 100 K with an incident energy $E_i = 29.7$ meV. The 1D plot in FIG.6(d) displays excitations at 2.9, 4.9, and 9.6 meV, which diminish at 30 K and completely vanish above the ordering temperature at 100 K, indicating the magnetic origin of these feature. Further, the intensity of these low-energy excitations decreases with increasing Q , as the magnetic form factor decreases with increasing Q . Hence, these excitations are characterized as magnon excitations.

We next examine the crystal electric field (CEF) excitations arising from Dy^{3+} . The contour plots of INS spectra with an incident neutron energy of $E_i = 180$ meV are shown in the FIG.7(a)–(c) for temperatures of 5 K, 30 K, and 100 K, respectively. At 100 K, excitations are observed at 46.5 meV and 71.8 meV in the Q region 1.5 to 4.0 \AA^{-1} . The 1D plot in FIG. 7(d) shows the CEF transitions at 5, 30, and 100 K. At 5 K, the 46.5 meV

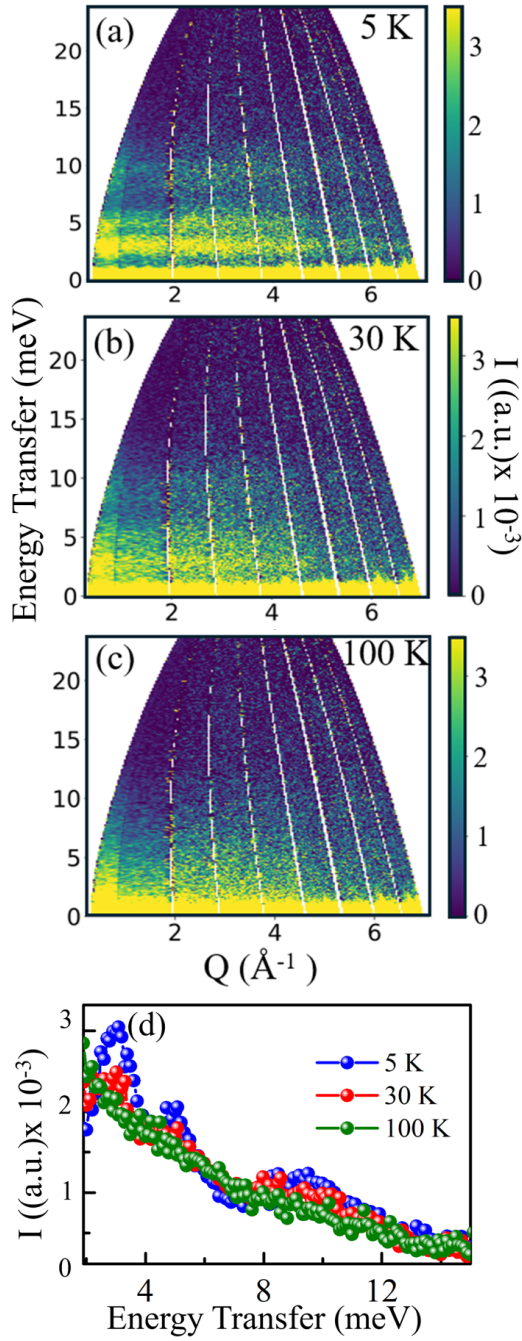


FIG. 6. (a-c) 2D contour color plots showing magnon excitations at 5 K, 30 K, and 100 K, respectively. (d) Comparison of magnon excitations (Intensity(I) vs. Energy Transfer) at various temperatures in the Q region 0.5 to 4.0 \AA^{-1} .

excitation shifts to 37.5 meV , possibly due to Zeeman splitting. Similar kind CEF excitations have also been reported for Dy^{3+} in the $\text{Sr}_2\text{DyRuO}_6$ system [34].

FIG. 8 presents a one-dimensional plot showing phonon excitations observed in the high- Q region 13 to 17 \AA^{-1} , consistent with the phonon spectral behavior where the phonon intensity increases with Q following

$I \propto Q^2$. FIG.8(a) displays excitations around 9 – 28 meV , 32 – 38 meV , 43 meV , 51 meV , and 66 – 74 meV for an incident energy of $E_i = 100 \text{ meV}$ at 5 K . For comparison and to probe higher energy ranges, FIG.8(b) shows data with $E_i = 180 \text{ meV}$, revealing the same phonon excitations along with a weak feature near 90 meV .

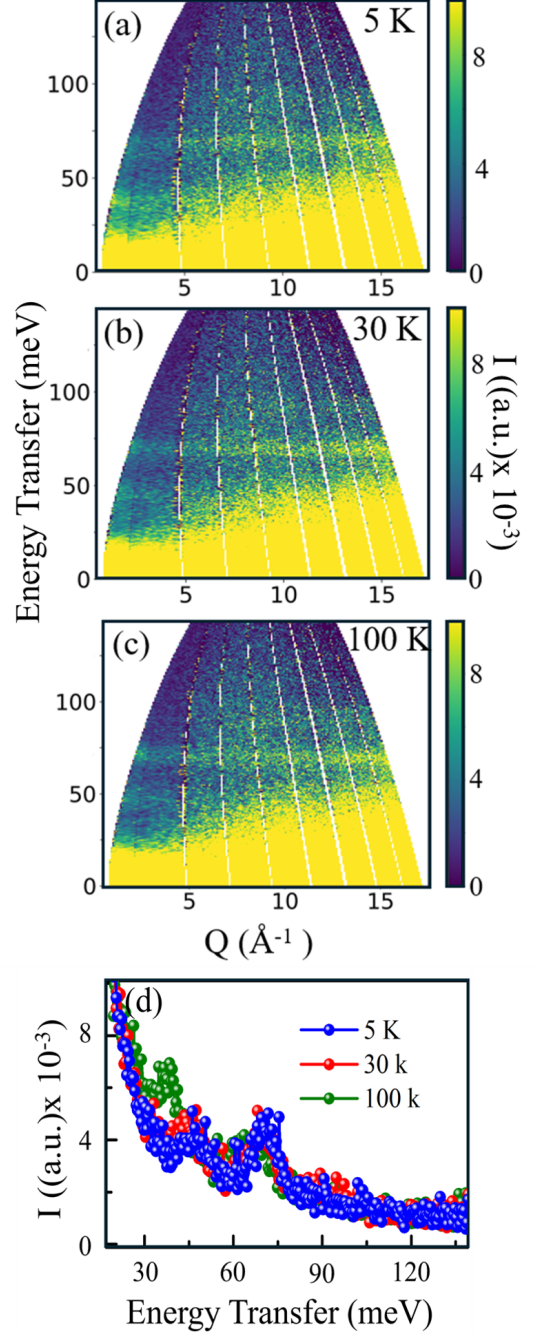


FIG. 7. (a-c) Color contour plots of crystal electric field (CEF) excitations at 5 K, 30 K, and 100 K, respectively. (d) Comparison of CEF excitations (Intensity(I) vs. Energy Transfer) at various temperatures in the Q region 1.5 to 4.0 \AA^{-1} .

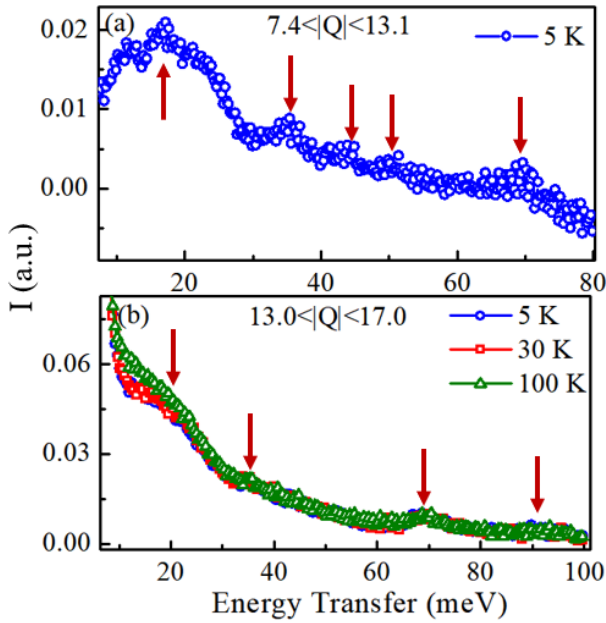


FIG. 8. (a) Phonon excitations (Intensity(I) vs. Energy Transfer) measured with $E_i = 100$ meV at $T = 5$ K in the Q range $13 \leq Q \leq 17$ \AA^{-1} . (b) Comparison of phonon excitations (intensity vs. energy transfer) measured with $E_i = 180$ meV at various temperatures in the same Q range.

1. SpinW: Theoretical modeling

The spin-spin exchange interaction and the nature of anisotropy in the system are investigated by developing a theoretical model with SPINW to generate the magnon excitation spectrum, which is shown in FIG.9(a). The spin Hamiltonian of the Heisenberg system includes the exchange interaction J and the single-ion anisotropy term D , expressed as

$$H = J \sum_{\langle ij \rangle} \vec{S}_i \cdot \vec{S}_j + D \sum_i (S_i^z)^2. \quad (1)$$

Here, J represents the exchange interaction between neighbouring magnetic atoms, and D denotes the anisotropy tensor [52]. From the simulations, the extracted J and D values are listed in TABLE II. The simulated magnon-dispersion curves and the corresponding contour plot of magnon spectra are shown in FIG.9(a) and FIG.9(b), respectively, which reveal clear excitations around 3, 5, and 10 meV that closely agrees the experimentally obtained magnon excitations from INS (see FIG.6(a)).

As shown in TABLE II, $J_{\text{Dy-Ru}} > J_{\text{Ru-Ru}} > J_{\text{Dy-Dy}}$. In BDRO, the long-range magnetic order is dominated by the Ru-O-Dy antiferromagnetic (AFM) interaction, which is absent in similar compounds [34], likely due to the large spatial separation and weak superexchange pathways. The Ru⁵⁺ ions strongly hybridize with Dy³⁺ through oxygen, forming a robust 180° superexchange

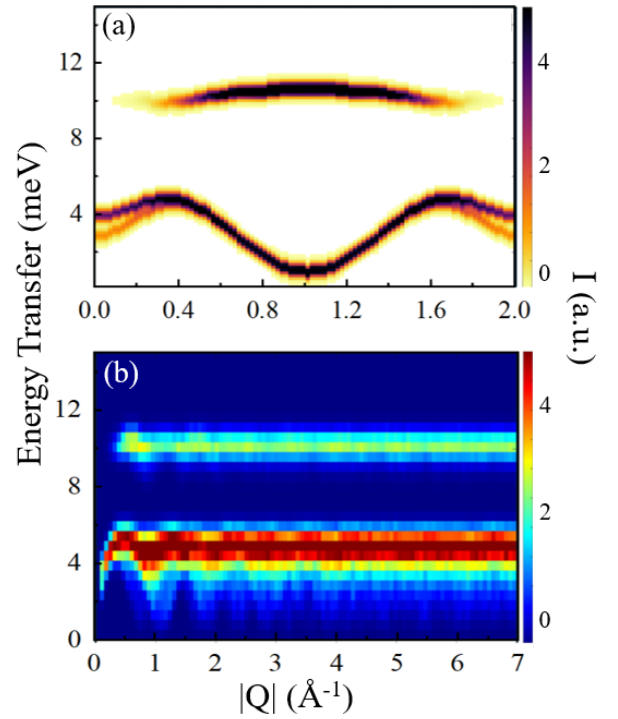


FIG. 9. (a) Spin-wave dispersion curve showing magnon excitations at approximately 3, 5, and 9 meV. (b) Energy vs. momentum-transfer plot showing the 3D color contour of powder average spin-wave intensity obtained from SPINW simulations.

path. In contrast, the Ru-Ru interaction proceeds via a super-superexchange pathway (Ru-O-Dy-O-Ru), which is comparatively weaker. Similarly, the Dy-Dy interaction follows the Dy-O-Ru-O-Dy super-superexchange pathway, which is extremely weak because the Dy 4f orbitals are highly localized, resulting in minimal overlap with the O 2p states.

The anisotropy 3×3 tensor contains only non-diagonal terms, specifically D_{zx} and D_{xz} (with $\mathbf{k} = (010)$ and collinear Ising moments lying in the ac -plane). Compared to the exchange interaction J , the D terms are not strong enough to dominate the spin interactions. The anisotropy matrix contains nonzero off-diagonal elements ($D_{xz} = D_{zx} = 0.10$), which causes the Ising-like moments to preferentially align within the ac -plane. In this case, determining the exact moment direction is not possible: if the spins were constrained to the ab plane, the corresponding nonzero elements would be $D_{xy} = D_{yx} = 0.10$; similarly, for moments lying in the bc plane, one would obtain $D_{yz} = D_{zy} = 0.10$. Inclusion of the anisotropy term is therefore essential to reproduce the correct spin orientation and the observed magnon excitations.

TABLE II. Exchange interactions and single-ion anisotropy used in the SPINW simulation, where nn and nnn refer to nearest and next-nearest-neighbour exchange, respectively. (Positive J denotes antiferromagnetic interaction, while negative J denotes ferromagnetic interaction.)

Parameter	Value (meV)
J_1 (nn Dy–Ru)	0.52
J_2 (nn Dy–Dy)	0.09
J_3 (nn Ru–Ru)	0.12
J_4 (nnn Dy–Ru)	−0.10

Anisotropy matrix D (meV):

$$D = \begin{bmatrix} 0 & 0 & 0.10 \\ 0 & 0 & 0 \\ 0.10 & 0 & 0 \end{bmatrix}$$

2. CEF Point Charge Calculation of Dy^{3+}

To interpret the crystal electric field (CEF) excitations theoretically, we employ point charge calculations. Here, we discuss the CEF splitting of Dy^{3+} ($4f^9$), which is in the O_h point group of $m\bar{3}m$ symmetry in cubic BDRO. For Dy^{3+} ($4f^9$) in O_h site symmetry, two doublets and four quartets are expected, yielding a total of 16 states (as $2J + 1 = 15/2 \times 2 + 1 = 16$) [53]. We now represent CEF excitation through the point charge model, where the CEF Hamiltonian for the Dy^{3+} site symmetry is given below,

$$\hat{H}_{\text{CEF}} = B_4^0 \hat{O}_4^0 + B_4^4 \hat{O}_4^4 + B_6^0 \hat{O}_6^0 + B_6^4 \hat{O}_6^4. \quad (2)$$

The single-ion crystal electric field (CEF) interaction is parametrized as a linear combination of the four symmetry-allowed Stevens operators, \hat{O}_n^m , for the O_h site symmetry of the DyO_6 octahedral environment [54].

The calculated Stevens parameters, B_4^0 and B_6^0 , obtained from the simulated results for Dy^{3+} in Ba_2DyRuO_6 , which are used to reproduce the measured CEF levels at 100 K, are listed in Table III. For cubic symmetry, $B_4^4 = 5B_4^0$ and $B_6^4 = -21B_6^0$ are related [55].

TABLE III. Stevens parameters B_n^m for Dy^{3+} in Ba_2DyRuO_6 at 100 K and 5 K.

Parameter	100 K (meV)	5 K (meV)
B_4^0	$-8.84(5) \times 10^{-4}$	$-1.43(6) \times 10^{-3}$
B_6^0	$8.30(6) \times 10^{-6}$	$-1.22(5) \times 10^{-5}$

The CEF excitations obtained from point-charge calculations reveal a ground-state doublet $|0\rangle$ at 0 meV, a first excited quartet $|1\rangle$ at 11.8 meV, a second excited doublet $|2\rangle$ at 14.3 meV, a third excited quartet $|3\rangle$ at 54.5 meV, and a fourth excited quartet $|4\rangle$ at 64.5 meV.

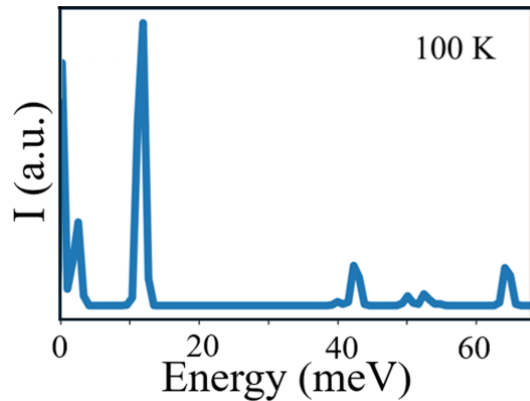


FIG. 10. Crystal field excitations calculated using the point charge model in the MANTID Crystal Field program at 100 K, within the paramagnetic region, with intensity (I) plotted as a function of energy (E).

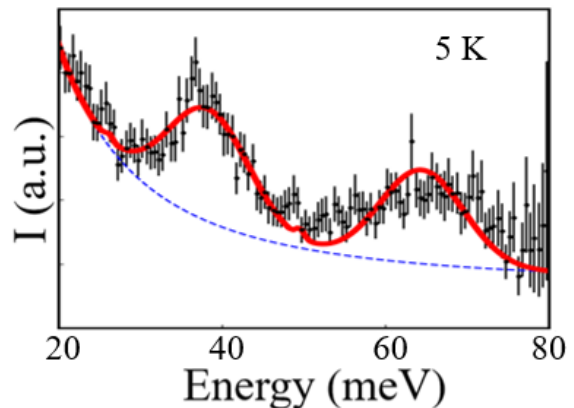


FIG. 11. Crystal electric field (CEF) fit to the 5 K inelastic neutron scattering spectrum of Dy^{3+} . The solid blue line represents the total fit consisting of the elastic peak and a linear background.

The intermediate-state transitions at 100 K are also visible due to thermal population, as shown in FIG. 10. The observed intermediate transitions correspond to the following states: $|1\rangle \rightarrow |2\rangle$ at 2.5 meV ((14.3–11.8) meV), $|1\rangle \rightarrow |3\rangle$ at 42.7 meV ((54.5–11.8) meV), $|1\rangle \rightarrow |4\rangle$ at 52.7 meV ((64.5–11.8) meV), $|2\rangle \rightarrow |3\rangle$ at 40.2 meV ((54.5–14.3) meV), and $|2\rangle \rightarrow |4\rangle$ at 50.2 meV ((64.5–14.3) meV), as shown in FIG. 10. Among these, the 42.7 meV ($|1\rangle \rightarrow |3\rangle$) and 64.5 meV ($|0\rangle \rightarrow |4\rangle$) transitions closely match the experimentally observed CEF excitations at 46.5 meV and 71.8 meV, respectively (see FIG. 7(c)).

It is noted that the ordered state moment from the point charge model is calculated as $\mu_{\text{ord}} = 5.7\mu_B$ for Dy^{3+} , which is close to the experimental value of $5.1(1)\mu_B$ (see FIG. 12(a)). The magnetic contribution of heat capacity, C_{mag} , obtained from this modelling is presented in FIG. 12(b), which shows a close agreement

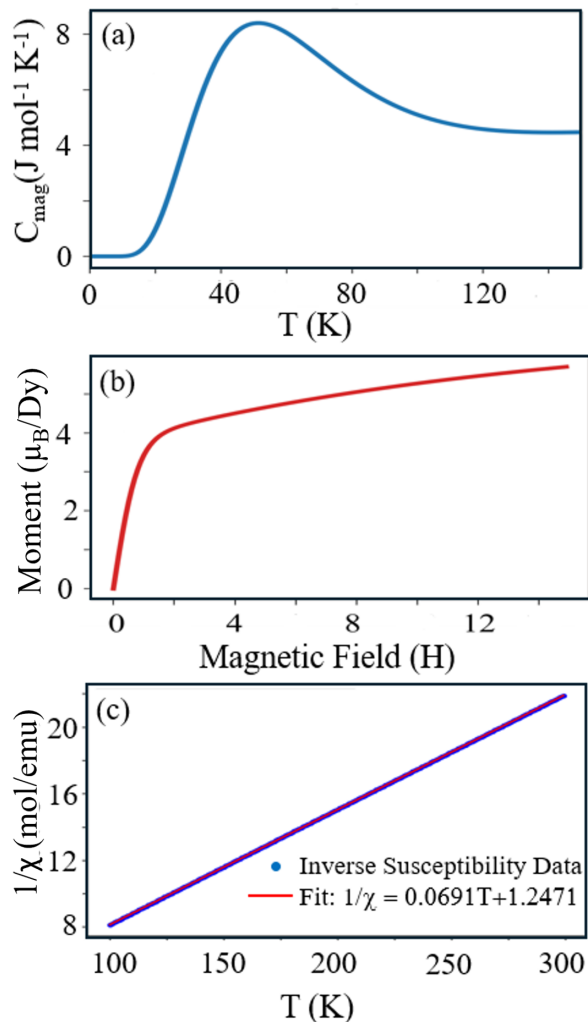


FIG. 12. Results from point charge theoretical calculations — (a) Magnetic heat capacity as a function of temperature T , (b) Dy^{3+} magnetic moment calculated as a function of applied magnetic field H , and (c) Curie–Weiss fit to the inverse magnetic susceptibility.

with the experimental C_{mag} versus T data. Additionally, the Curie–Weiss fit of inverse susceptibility versus temperature, based on this theoretical calculation, yields $\Theta_{\text{cp}} \approx -17.33$ K and a paramagnetic moment $\mu_{\text{Dy}} \approx 10.75\mu_B$, (FIG. 12c) both of which are in close agreement with experimental results [29]. The ground state wavefunctions are found as,

$$|\psi_0\rangle = 0.23 \left| \mp \frac{11}{2} \right\rangle + 0.45 \left| \mp \frac{3}{2} \right\rangle - 0.58 \left| \pm \frac{5}{2} \right\rangle - 0.63 \left| \pm \frac{13}{2} \right\rangle.$$

The point charge model is an approximation and does not provide an accurate ground eigenstate, but it depicts that the $\left| \frac{13}{2} \right\rangle$ wavefunction contributes the most. It also predicts the energy gap of the crystal electric field (CEF) excitation between the Kramers doublets. In the paramagnetic region, we observe 8 CEF excitations as expected through point charge model as shown in FIG 10. The

observation of only two CEF excitations experimentally may be attributed to the weak population of most CEF levels in the paramagnetic region and to thermal broadening, which can merge closely spaced excitations into broad peaks, thereby reducing their visibility in INS [56].

Crystal electric field (CEF) fitting was carried out on the 5 K CEF excitations (see FIG. 7(a)) of the Dy^{3+} ion in the DAaaS system, as shown in FIG. 11. The fitted Stevens parameters for 5K are shown in Table III. Equivalently, within the Lea–Leask–Wolf (LLW) formalism, the corresponding parameters are $x = 0.340 \pm 0.02$ and $W = -0.257 \pm 0.01$ meV.

From the CEF fitting, a total of 16 energy levels are obtained, consistent with the $J = 15/2$ multiplet of Dy^{3+} . The level scheme consists of a quartet ground state, followed by a first excited doublet at 38.2 meV, a second excited quartet at 64.4 meV, a third excited quartet at 87.8 meV, and a fourth excited doublet at 111.8 meV. The excitations at 38.2 and 64.4 meV closely match the experimentally observed CEF excitations, as shown in Fig. 7(a) and Fig. 7(d). The ground-state quartet wavefunctions, expressed in the $|m_J\rangle$ basis, are given by

$$\begin{aligned} |\psi_0\rangle &= -0.74 \left| \mp \frac{15}{2} \right\rangle + 0.58 \left| \mp \frac{7}{2} \right\rangle + 0.32 \left| \pm \frac{1}{2} \right\rangle + 0.03 \left| \pm \frac{9}{2} \right\rangle, \\ &= \pm 0.12 \left| \mp \frac{11}{2} \right\rangle \mp 0.63 \left| \mp \frac{3}{2} \right\rangle \mp 0.71 \left| \pm \frac{5}{2} \right\rangle \pm 0.25 \left| \pm \frac{13}{2} \right\rangle. \end{aligned}$$

Although the ground state is predominantly composed of the $|m_J| = 15/2$ components, a significant admixture from lower $|m_J|$ states is observed. This indicates a deviation from the ideal Ising limit while retaining strong single-ion anisotropy for the Dy^{3+} ion.

C. Raman Spectroscopy

In $\text{Ba}_2\text{DyRuO}_6$, the Wyckoff positions of Ba, Dy, Ru, and O are $8c$, $4b$, $4a$, and $24e$, respectively, corresponding to site symmetries T_d , O_h , and C_{4v} . Since the system possesses a centrosymmetric space group, the Raman-active modes are infrared-inactive. The Raman active modes are summarised in Table IV, with the help of the Bibao crystallographic server [57].

Here the T_{2u} and T_{1u} modes are inactive in Raman spectra but can be observed via hyper-Raman scattering. In FIG 13, our Raman spectra at 300 K show peaks at 341 cm^{-1} (42 meV), 443 cm^{-1} (55 meV), 555 cm^{-1} (69 meV), and 747 cm^{-1} (92 meV). All these existing peaks are also observed in the INS data at 100 K. Based on comparison with the INS data, the peaks at 341 cm^{-1} (~ 42 meV) and 555 cm^{-1} (~ 69 meV) are assigned to crystal electric field (CEF) excitations (see FIG. 7(d)), with phonon modes also observable in this range. The peaks at 443 cm^{-1} (~ 55 meV) and 747 cm^{-1} (~ 92 meV) are attributed to pure phonon modes (see FIG. 8).

TABLE IV. Raman Active Modes

$$\Gamma = A_{1g} + E_g + 2T_{2g}$$

WP	A_{1g}	E_g	T_{2g}
Ba (8c)	.	.	1
Dy (4b)	.	.	.
Ru (4a)	.	.	.
O (24e)	1	1	2

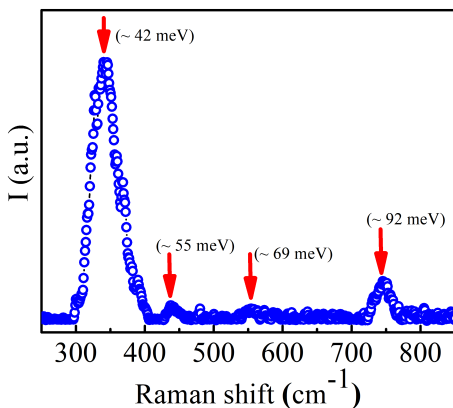


FIG. 13. Raman spectra of $\text{Ba}_2\text{DyRuO}_6$ recorded at 300 K, with Intensity (I) plotted as a function of Raman shift (cm^{-1}), showing the characteristic vibrational modes.

D. Machine Learning Models for Phonon Excitation

We calculated the phonons across the full $|Q|$ -range to separate the phonons with the magnetic signals seen in the INS data [47, 48]. For this, we used the 5 K crystal structure and optimised the structure. FIG. 14(a) shows the calculated phonon spectrum that spans up to 25 THz and shows no imaginary frequencies, confirming the dynamic stability of the optimised structure. After getting this, we calculated the powder-averaged neutron scattering intensity convolved with the instrumental energy and momentum resolution. This calculation also included multiple phonon processes and temperature-dependent thermal population of phonons. The simulated intensity (FIG. 13(b)) shows that phonon scattering dominates the $|Q|$ region 7.4 to 17 \AA^{-1} , consistent with the measured phonon cross sections. This calculation shows the low-energy excitations that appear broad and unresolved in the experimental INS data below 52 meV (see FIG. 8(a)), due to both the closely spaced modes and the instrumental energy resolution in this vicinity

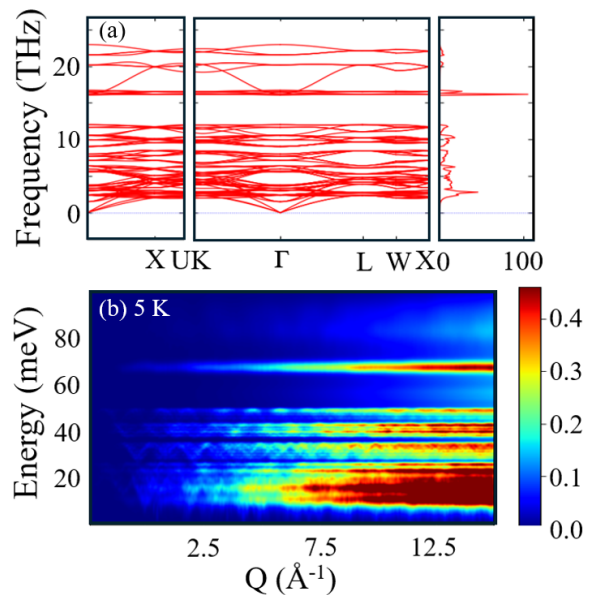


FIG. 14. (a) Calculated phonon modes for $\text{Ba}_2\text{DyRuO}_6$ based upon pre-trained machine learning force fields. Vertical axis is the phonon energy in units of THz. Panels indicate wave-vector dependence in reciprocal space using standard reciprocal space, (b) Calculated phonon scattering intensity at 5 K

of energy transfer. The simulated spectrum allows us to identify well-separated phonon excitations in the range 9-28 meV, 32-38 meV, 43 meV, 51 meV, and 66-74 meV, along with an additional weaker excitation near 90 meV. These calculated energies match very well with the excitations observed in the experimental spectra (see FIG. 8), confirming both the accuracy of the phonon calculation and its consistency with the experimental INS results. Such a clear agreement between the INS experimental phonon spectra and the theoretical MLFF simulated phonon spectra is also observed in another ruthenate system [52]. The calculated powder intensity also makes clear that the experimentally observed Dy^{3+} CEF levels overlap in energy with phonon branches, providing further motivation to extend future measurements to look for coupling between the CEF and lattice degrees of freedom.

IV. CONCLUSION

Experimental and theoretical investigations reveal the magnetic ground state of $\text{Ba}_2\text{DyRuO}_6$ and the mechanisms underlying its magnetic and lattice excitations. Time-of-flight neutron diffraction shows a long-range antiferromagnetic order below $\sim 47(1)$ K, with Ru^{5+} and Dy^{3+} moments collinearly aligned, exhibiting nearly Ising-like anisotropy. Inelastic neutron scattering detects sharp Dy-Ru magnon modes arising from strong $4d$ - $4f$ exchange, alongside distinct Dy^{3+} crystal-electric-field excitations, which a point-charge model well cap-

tures. Raman spectroscopy confirms the key phonon modes and the CEF excitation. SpinW modelling of spin wave quantifies the dominant Dy–Ru exchange interactions and weak off-diagonal anisotropy, providing microscopic insight into the origin of the ground state and the magnon spectrum, which is rare in this family of systems. Furthermore, machine-learning-based force-field calculations accurately reproduce the momentum-dependent phonon modes observed in INS. Collectively, these results demonstrate that $4d$ – $4f$ hybridisation and subtle single-ion anisotropy govern the quasiparticle dynamics in $\text{Ba}_2\text{DyRuO}_6$. Also, there is a significant overlap between the crystal electric field and lattice excitations in this compound. This motivates further efforts to determine conclusively whether these degrees of freedom are interacting. Non-magnetic substitution on the A sites may provide a mechanism to tune exchange interactions in the A_2RRuO_6 double perovskites. This diverse set of materials offers numerous routes for the design of quantum materials with bespoke properties.

V. ACKNOWLEDGEMENTS

T.B. acknowledges funding support from the Science and Engineering Research Board (SERB) (Anusandhan National Research Foundation (ANRF)), Government of India (Project No. SRG/2022/000044), and the UGC-DAE Consortium for Scientific Research (CSR) (Project No. CRS/2021-22/03/544), as well as the SEED Grant from RGIPT. TB thanks the Science and Technology Facilities Council (STFC, UK) for providing neutron beam time on the WISH (proposal #RB2368022, DOI: 10.5286/ISIS.E.RB2368022-1) and MARI (proposal

#RB2490022, DOI: 10.5286/ISIS.E.RB2490022-1) instruments at the ISIS Neutron and Muon Source. The corresponding raw data underlying this study can be accessed at the given DOI links. TB gratefully acknowledges financial support from the Department of Science and Technology, India, for access to the experimental facility at STFC and financial support to experiment with the DST-RAL project, and Jawaharlal Nehru Centre for Advanced Scientific Research (JNCASR) for managing this funding as the Nodal Office. TB thanks the Oak Ridge National Laboratory (ORNL) for providing access to the computational facilities for machine-learning-based on phonon calculations. TB thanks the Central Instrumentation Facilities (CIF), RGIPT. Computational analysis of spin-wave dispersions using SpinW was carried out with support from the MATLAB academic license at RGIPT. M.B. S. acknowledge support from the U.S. Department of Energy (DOE), Office of Science, Basic Energy Sciences, Scientific User Facilities Division. D.T.A. acknowledges EPSRC UK (Grant Ref: EP/W00562X/1) for funding. J.S. would like to thank SERB, DST-India, for the Ramanujan Fellowship (Grant No. RJF/2019/000046). M.K. thanks the University Grants Commission (UGC), India, for the research fellowship.

COMPETING INTERESTS

The authors declare no competing financial interests.

REFERENCES

-
- [1] S. Lee, A. Pirogov, M. Kang, K. H. Jang, M. Yonemura, T. Kamiyama, S.-W. Cheong, F. Gozzo, N. Shin, H. Kimura, and Y. Noda, “Giant magneto-elastic coupling in multiferroic hexagonal manganites,” *Nature* **451**, 805 (2008).
 - [2] J. Hwang, E. S. Choi, F. Ye, C. R. Dela Cruz, Y. Xin, H. D. Zhou, and P. Schlottmann, “Successive magnetic phase transitions and multiferroicity in the spin-one triangular-lattice antiferromagnet $\text{Ba}_3\text{NiNb}_2\text{O}_9$,” *Phys. Rev. Lett.* **109**, 257205 (2012).
 - [3] T. Basu, V. Caignaert, S. Ghara, X. Ke, A. Pautrat, S. Krohns, A. Loidl, and B. Raveau, “Enhancement of magnetodielectric coupling in 6H-perovskites $\text{Ba}_3\text{R Ru}_2\text{O}_9$ for heavier rare-earth cations (R = Ho, Tb),” *Phys. Rev. Mater.* **3**, 114401 (2019).
 - [4] H. You, Y. Zhang, J. Chen, N. Ding, M. An, L. Miao, and S. Dong, “Peierls transition driven ferroelasticity in the two-dimensional d-f hybrid magnets,” *Phys. Rev. B* **103**, L161408 (2021).
 - [5] A. Dönni, V. Y. Pomjakushin, K. Yamaura, and A. A. Belik, “Cycloidal spiral magnetic structures in the spin-chain compounds BaRFeO_4 (R = Yb and Tm): Ordered Yb versus partly ordered Tm,” *Phys. Rev. B* **107**, 134412 (2023).
 - [6] R. Bag, S. Xu, N. E. Sherman, L. Yadav, A. I. Kolesnikov, A. A. Podlesnyak, E. S. Choi, I. Da Silva, J. E. Moore, and S. Haravifard, “Evidence of Dirac quantum spin liquid in $\text{YbZn}_2\text{GaO}_5$,” *Phys. Rev. Lett.* **133**, 266703 (2024).
 - [7] D. Slobinsky, C. Castelnovo, R. A. Borzi, A. S. Gibbs, A. P. Mackenzie, R. Moessner, and S. A. Grigera, “Unconventional magnetization processes and thermal runaway in spin-ice $\text{Dy}_2\text{Ti}_2\text{O}_7$,” *Phys. Rev. Lett.* **105**, 267205 (2010).
 - [8] S. N. Gordeev, J.-M. Beaujour, G. J. Bowden, B. D. Rainford, P. A. J. de Groot, R. C. C. Ward, M. R. Wells, and A. G. M. Jansen, “Giant magnetoresistance by exchange springs in $\text{DyFe}_2/\text{YFe}_2$ superlattices,” *Phys. Rev. Lett.* **87**, 186808 (2001).
 - [9] A. Rauguth, A. Alhassanat, H. Elnaggar, A. A. Athanassopoulou, C. Luo, H. Ryll, F. Radu, T. Mashoff, F. M. de Groot, E. Rentschler, and H. J. Elmers, “Anisotropy of 4f states in 3d-4f single-molecule magnets,” *Phys. Rev. B* **105**, 134415 (2022).

- [10] C. Huang, R. Sun, L. Bao, X. Tian, C. Pan, M. Li, W. Shen, K. Guo, B. Wang, X. Lu, and S. Gao, "A hard molecular nanomagnet from confined paramagnetic 3d–4f spins inside a fullerene cage," *Nat. Commun.* **14**, 8443 (2023).
- [11] T. Basu, V. Caignaert, F. Damay, T. W. Heitmann, B. Raveau, and X. Ke, "Cooperative Ru(4d)–Ho(4f) magnetic ordering and phase coexistence in the 6H perovskite multiferroic Ba₃HoRu₂O₉," *Phys. Rev. B* **102**, 020409(R) (2020).
- [12] E. Kushwaha, G. Roy, A. M. dos Santos, M. Kumar, S. Ghosh, T. Heitmann, and T. Basu, "Unconventional S-orbital state of Tb and cooperative Ru(4d)–Tb(4f) spin ordering in the strongly correlated 4d–4f system Ba₃TbRu₂O₉," *J. Mater. Chem. C* **13**, 15384 (2025).
- [13] D. Ziat, A. A. Aczel, R. Sinclair, Q. Chen, H. D. Zhou, T. J. Williams, M. B. Stone, A. Verrier, and J. A. Quilliam, "Frustrated spin- $\frac{1}{2}$ molecular magnetism in the mixed-valence antiferromagnets Ba₃MRu₂O₉ (M = In, Y, Lu)," *Phys. Rev. B* **95**, 184424 (2017).
- [14] E. Granado, J. W. Lynn, R. F. Jardim, and M. S. Torikachvili, "Two-dimensional magnetic correlations and partial long-range order in geometrically frustrated Sr₂YRuO₆," *Phys. Rev. Lett.* **110**, 017202 (2013).
- [15] N. Taira, M. Wakeshima, and Y. Hinatsu, "Magnetic properties of ruthenium pyrochlores R₂Ru₂O₇ (R = rare earth)," *J. Phys.: Condens. Matter* **11**, 6983 (1999).
- [16] J. S. Lee, T. W. Noh, J. S. Bae, I. S. Yang, T. Takeda, and R. Kanno, "Strong spin-phonon coupling in the geometrically frustrated pyrochlore Y₂Ru₂O₇," *Phys. Rev. B* **69**, 214428 (2004).
- [17] F. Mueur, J. Robert, F. Morineau, V. Simonet, E. Pachoud, A. Hadj-Azzem, C. Colin, P. Manuel, J. R. Stewart, P. C. W. Holdsworth, and E. Lhotel, "Ferromagnetic fragmented ground state in the pyrochlore Ho₂Ru₂O₇," arXiv:2411.10078 (2024).
- [18] T. Basu, V. Caignaert, S. Ghara, X. Ke, A. Pautrat, S. Krohns, A. Loidl, and B. Raveau, "Enhancement of magnetodielectric coupling in 6H-perovskites Ba₃R Ru₂O₉ for heavier rare-earth cations (R = Ho, Tb)," *Phys. Rev. Mater.* **3**, 114401 (2019).
- [19] E. Kushwaha, G. Roy, M. Kumar, A. M. dos Santos, S. Ghosh, D. T. Adroja, V. Caignaert, O. Perez, A. Pautrat, and T. Basu, "Origin of spin-driven ferroelectricity and effect of external pressure on the complex magnetism of the 6H perovskite Ba₃HoRu₂O₉," *Phys. Rev. B* **109**, 224418 (2024).
- [20] M. S. Senn, S. A. J. Kimber, A. M. Arevalo Lopez, A. H. Hill, and J. P. Attfield, "Spin orders and lattice distortions of geometrically frustrated 6H-perovskites Ba₃B'(Ru₂O₉) (B' = La³⁺, Nd³⁺, and Y³⁺)," *Phys. Rev. B* **87**, 134402 (2013).
- [21] K. I. Kobayashi, T. Kimura, H. Sawada, K. Terakura, and Y. Tokura, "Room-temperature magnetoresistance in an oxide material with an ordered double-perovskite structure," *Nature* **395**, 677 (1998).
- [22] T. Dey, A. Maljuk, D. V. Efremov, O. Kataeva, S. Gass, C. G. F. Blum, F. Steckel, D. Gruner, T. Ritschel, A. U. B. Wolter, and J. Geck, "Ba₂YIrO₆: A cubic double perovskite material with Ir⁵⁺ ions," *Phys. Rev. B* **93**, 014434 (2016).
- [23] G. J. Nilsen, C. M. Thompson, C. Marjerrison, D. I. Badrtdinov, A. A. Tsirlin, and J. E. Greedan, "Magnetic order and multipoles in the 5d² rhenium double perovskite Ba₂YReO₆," *Phys. Rev. B* **103**, 104430 (2021).
- [24] M. M. Isah, B. Dalal, X. Kang, D. F. Mosca, I. J. Onuorah, V. Scagnoli, P. Bonfà, R. De Renzi, A. A. Belik, C. Franchini, and K. Yamaura, "Magnetic behavior of 5d¹ Re-based double perovskite Sr₂ZnReO₆," arXiv:2509.04071 (2025).
- [25] V. da Cruz Pinha Barbosa, D. D. Maharaj, Z. W. Cronkright, Y. Wang, R. Cong, E. Garcia, A. P. Reyes, J. Yan, C. Ritter, V. F. Mitrović, and B. D. Gaulin, "Exploring the links between structural distortions, orbital ordering, and multipolar magnetic ordering in double perovskites containing Re(VI) and Os(VII)," *Chem. Mater.* **36**, 11478 (2024).
- [26] A. S. Erickson, S. Misra, G. J. Miller, R. R. Gupta, Z. Schlesinger, W. A. Harrison, J. M. Kim, and I. R. Fisher, "Ferromagnetism in the Mott insulator Ba₂NaOsO₆," *Phys. Rev. Lett.* **99**, 016404 (2007).
- [27] L. V. Pourvskii, D. Fiore Mosca, L. Celiberti, S. Khmelevskiy, A. Paramekanti, and C. Franchini, "Hidden orders in spin-orbit-entangled correlated insulators," *Nat. Rev. Mater.* (2025).
- [28] Y. Hinatsu and Y. Doi, "Structures and magnetic properties of double perovskites A₂LnMO₆ and 6H-perovskites Ba₃LnRu₂O₉ (A = Sr, Ba; Ln = Y, lanthanides; M = Nb, Ta, Ru)," *Bull. Chem. Soc. Jpn.* **76**, 1093 (2003).
- [29] R. Kumar, C. V. Tomy, R. Nagarajan, P. L. Paulose, and S. K. Malik, "Magnetization and heat capacity studies of double perovskite compounds Ba₂SmRuO₆ and Ba₂DyRuO₆," *Physica B* **404**, 2369 (2009).
- [30] Y. Hinatsu, Y. Izumiyama, Y. Doi, A. Alemi, M. Wakeshima, A. Nakamura, and Y. Morii, "Studies on magnetic and calorimetric properties of double perovskites Ba₂HoRuO₆ and Ba₂HoIrO₆," *J. Solid State Chem.* **177**, 38 (2004).
- [31] Sannigrahi, J., Adroja, D. T., Ritter, C., Kockelmann, W., Hillier, A. D., Knight, K. S., Boothroyd, A. T., Wakeshima, M., Hinatsu, Y., Mosselmans, J. F. W., and Ramos, S., 2019. First-order valence transition: Neutron diffraction, inelastic neutron scattering, and x-ray absorption investigations on the double perovskite Ba₂PrRu_{0.9}Ir_{0.1}O₆. *Phys. Rev. B* **99**, 184440.
- [32] Mohanty, P., Marik, S., Singh, D., and Singh, R. P., 2017. Exchange bias properties in Sr₂LnRuO₆ (Ln = Dy, Ho and Er). *Mater. Res. Express* **4**, 126103.
- [33] Parkinson, N. G., Hatton, P. D., Howard, J. A., Ritter, C., Ibberson, R. M., and Wu, M. K., 2004. Variable temperature neutron powder diffraction study to determine the magnetic interactions in Sr₂LnRuO₆ (Ln = Ho and Tb). *J. Phys.: Condens. Matter* **16**, 7611.
- [34] Adroja, D. T., Sharma, S., Ritter, C., Hillier, A. D., Le, D., Tomy, C. V., Singh, R., Smith, R. I., Koza, M., Sundaresan, A., and Langridge, S., 2020. Muon spin rotation and neutron scattering investigations of the B-site ordered double perovskite Sr₂DyRuO₆. *Phys. Rev. B* **101**, 094413.
- [35] Sáez-Puche, R., Climent-Pascual, E., Ruiz-Bustos, R., Alario-Franco, M. A., and Fernández-Díaz, M. T., 2007. Non-collinear magnetic structure of the Sr₂ErRuO₆ double perovskite. *Prog. Solid State Chem.* **35**, 211–219.
- [36] Aharen, T., Greedan, J. E., Ning, F., Imai, T., Michaelis, V., Kroeker, S., Zhou, H., Wiebe, C. R., and Cranswick, L. M., 2009. Magnetic properties of the S = 3/2 geometrically frustrated double perovskites La₂LiRuO₆ and Ba₂YRuO₆. *Phys. Rev. B* **80**, 134423.

- [37] Sharma, S., Adroja, D. T., Ritter, C., Khalyavin, D., Manuel, P., Stenning, G. B., Sundaresan, A., Hillier, A. D., Deen, P. P., Khomskii, D. I., and Langridge, S., 2020. Magnetic ground state of the ordered double perovskite $\text{Sr}_2\text{YbRuO}_6$: Two magnetic transitions. *Phys. Rev. B* **102**, 134412.
- [38] Tóth, S., and Lake, B., 2015. Linear spin wave theory for single- Q incommensurate magnetic structures. *J. Phys.: Condens. Matter* **27**, 166002.
- [39] Rodríguez-Carvajal, J., 1993. Recent advances in magnetic structure determination by neutron powder diffraction. *Physica B* **192**, 55–69.
- [40] Chapon, L. C., Manuel, P., Radaelli, P. G., Benson, C., Perrott, L., Ansell, S., Rhodes, N. J., Raspino, D., Duxbury, D., Spill, E., and Norris, J., 2011. WISH: The new powder and single-crystal magnetic diffractometer on the second target station. *Neutron News* **22**, 22–25.
- [41] Rodríguez-Carvajal, J., *BASIREPS: A program for calculating irreducible representations of space groups and basis functions for axial and polar vector properties*. Part of the FullProf Suite, available at <http://www.ill.eu/sites/fullprof/>.
- [42] Momma, K., and Izumi, F., 2011. VESTA 3 for three-dimensional visualization of crystal, volumetric and morphology data. *J. Appl. Cryst.* **44**, 1272–1276.
- [43] J. M. Perez-Mato, S. V. Gallego, E. S. Tasci, L. Elcoro, G. de la Flor, and M. I. Aroyo, *Annu. Rev. Mater. Res.* **45**, 217 (2015).
- [44] Le, M. D., Guidi, T., Bewley, R., Stewart, J. R., Schoonveld, E. M., Raspino, D., Pooley, D. E., Boxall, J., Gascoyne, K. F., Rhodes, N. J., and Moorby, S. R., 2023. Upgrade of the MARI spectrometer at ISIS. *Nucl. Instrum. Methods Phys. Res. A* **1056**, 168646.
- [45] Menk, R. H., Sharma, A., Vacchi, A., Besch, H. J., and Walenta, A., 2003. *Nucl. Instrum. Methods Phys. Res. A*, **508**, 478–483.
- [46] Azuah, R. T., Kneller, L. R., Qiu, Y., Tregenna-Piggott, P. L., Brown, C. M., Copley, J. R., and Dimeo, R. M., 2009. DAVE: A comprehensive software suite for the reduction, visualization, and analysis of low energy neutron spectroscopic data. *J. Res. Natl. Inst. Stand. Technol.* **114**, 341–358.
- [47] Yang, H., Hu, C., Zhou, Y., Liu, X., Shi, Y., Li, J., Li, G., Chen, Z., Chen, S., Zeni, C., and Horton, M., 2024. MatterSim: A deep learning atomistic model across elements, temperatures and pressures. *arXiv:2405.04967*.
- [48] Cheng, Y., Wu, G., Pajeroski, D. M., Stone, M. B., Savici, A. T., Li, M., and Ramirez-Cuesta, A. J., 2023. Direct prediction of inelastic neutron scattering spectra from the crystal structure. *Mach. Learn.: Sci. Technol.* **4**, 015010.
- [49] Aroyo, M. I., Orobengoa, D., de la Flor, G., Tasci, E. S., Perez-Mato, J. M., and Wondratschek, H., 2014. Brillouin-zone database on the Bilbao Crystallographic Server. *Acta Crystallogr. A* **70**, 126–137.
- [50] Perez-Mato, J. M., Gallego, S. V., Tasci, E. S., Elcoro, L., de la Flor, G., and Aroyo, M. I., 2015. Symmetry-based computational tools for magnetic crystallography. *Annu. Rev. Mater. Res.* **45**, 217–248.
- [51] Ding, L., Hu, C., Feng, E., Jiang, C., Kibalin, I. A., Gukasov, A., Chi, M., Ni, N., and Cao, H., 2021. Neutron diffraction study of magnetism in van der Waals layered $\text{MnBi}_2\text{Te}_{3n+1}$. *J. Phys. D: Appl. Phys.* **54**, 174003.
- [52] Kushwaha, E., Ghosh, S., Sannigrahi, J., Roy, G., Kumar, M., Cottrell, S., Stone, M. B., Fang, Y., Adroja, D. T., Ke, X., and Basu, T., 2025. Interplay between trimer structure and magnetic ground state in $\text{Ba}_5\text{Ru}_3\text{O}_{12}$ probed by neutron and μSR techniques. *Phys. Rev. B* **112**, 094410.
- [53] Lea, K. R., Leask, M. J. M., and Wolf, W. P., 1962. The raising of angular momentum degeneracy of f-electron terms by cubic crystal fields. *J. Phys. Chem. Solids* **23**, 1381–1405.
- [54] Jensen, J., and Mackintosh, A. R., 1991. *Rare Earth Magnetism: Structures and Excitations*. Oxford University Press, Oxford.
- [55] Lea, K. R., Leask, M. J. M., and Wolf, W. P., 1962. The raising of angular momentum degeneracy of f-electron terms by cubic crystal fields. *J. Phys. Chem. Solids* **23**, 1381–1405.
- [56] Passos, F. D. A., Nilsen, G. J., Patrick, C. E., Le, M. D., Balakrishnan, G., Kumar, S., Thamizhavel, A., Cornejo, D. R., and Jiménez, J. L., 2023. Inelastic neutron scattering investigation of the crystal field excitations of NdCo_5 . *Phys. Rev. B* **108**, 174409.
- [57] Kroumova, E., Aroyo, M. I., Perez-Mato, J. M., Kirov, A., Capillas, C., Ivantchev, S., and Wondratschek, H., 2003. Bilbao Crystallographic Server: Useful databases and tools for phase-transition studies. *Phase Transitions* **76**, 155–170.